






Virtual injections using 4D flow MRI with displacement corrections and constrained probabilistic streamlines

Grant S. Roberts¹  | Michael W. Loecher²  | Alma Spahic¹ | Kevin M. Johnson^{1,3}  | Patrick A. Turski³ | Laura B. Eisenmenger³  | Oliver Wieben^{1,3} 

¹Department of Medical Physics, University of Wisconsin—Madison, Madison, Wisconsin, USA

²Department of Radiology, Stanford University, Stanford, California, USA

³Department of Radiology, University of Wisconsin—Madison, Madison, Wisconsin, USA

Correspondence

Oliver Wieben, Department of Medical Physics, Wisconsin Institutes for Medical Research, 1111 Highland Avenue, Room 1005, Madison, WI 53705-2275, USA.
Email: owieben@wisc.edu

Funding information

National Institute on Aging, Grant/Award Number: F31AG071183 and P30AG062715; National Institute of Neurological Disorders and Stroke, Grant/Award Number: R01NS066982; National Center for Advancing Translational Sciences, Grant/Award Number: KL2TR002374 and UL1TR002373; American Heart Association, Grant/Award Number: 12PRE12080073

Abstract

Purpose: Streamlines from 4D-flow MRI have been used clinically for intracranial blood-flow tracking. However, deterministic and stochastic errors degrade streamline quality. The purpose of this study is to integrate displacement corrections, probabilistic streamlines, and novel fluid constraints to improve selective blood-flow tracking and emulate “virtual bolus injections.”

Methods: Both displacement artifacts (deterministic) and velocity noise (stochastic) inherently occur during phase-contrast MRI acquisitions. Here, two displacement correction methods, single-step and iterative, were tested in silico with simulated displacements and were compared with ground-truth velocity fields. Next, the effects of combining displacement corrections and constrained probabilistic streamlines were performed in 10 healthy volunteers using time-averaged 4D-flow data. Measures of streamline length and depth into vasculature were then compared with streamlines generated with no corrections and displacement correction alone using one-way repeated-measures analysis of variance and Friedman’s tests. Finally, virtual injections with improved streamlines were generated for three intracranial pathology cases.

Results: Iterative displacement correction outperformed the single-step method in silico. In volunteers, the combination of displacement corrections and constrained probabilistic streamlines allowed for significant improvements in streamline length and increased the number of streamlines entering the circle of Willis relative to streamlines with no corrections and displacement correction alone. In the pathology cases, virtual injections with improved streamlines were qualitatively similar to dynamic arterial spin labeling images and allowed for forward/reverse selective flow tracking to characterize cerebrovascular malformations.

Grant S. Roberts and Michael W. Loecher contributed equally to this work.

Conclusion: Virtual injections with improved streamlines from 4D-flow MRI allow for flexible, robust, intracranial flow tracking.

KEYWORDS

4D flow MRI, angiography, blood flow tracking, displacement correction, intracranial, probabilistic streamlines

1 | INTRODUCTION

Four-dimensional flow MRI is a noninvasive imaging method capable of obtaining time-averaged or time-resolved, three-directional velocity fields with volumetric coverage.¹ This type of acquisition provides vascular morphology, quantitative hemodynamic information, and allows for blood flow visualization, making it well-suited to study macrovascular anatomy and hemodynamics in multiple vessel segments. One common method to visualize 4D-flow MRI data is through the use of streamlines, which trace the path of a simulated massless particle over multiple, discrete time steps in the presence of a constant velocity field.^{2,3} Streamlines have been used for qualitatively assessing blood-flow patterns or abnormalities, such as flow jets and vortices, or in complex vascular territories.^{4–6} However, streamlines can also be used to selectively track the passage of blood, thereby emulating a “virtual bolus injection,” which may be useful in the study of cerebrovascular pathologies, like intracarotid plaques,⁷ or the characterization of vascular malformations^{8,9} and aneurysms.^{10,11}

Alternative methods for intracranial blood-flow tracking include digital subtraction angiography (DSA) and dynamic MRA with arterial spin labeling (ASL)¹² or contrast-enhanced MRI.¹³ Digital subtraction angiography (DSA) allows for the tracking of an arterial injection of iodinated contrast with high spatial and temporal resolution and is the gold standard for visualizing and diagnosing intracranial malformations.^{14,15} However, it carries risk in the form of procedural complications, radiation exposure, and adverse reactions to contrast agents.¹⁶ Arterial spin labeling and contrast-enhanced MRI are noninvasive methods that also show the path of blood flow following tagging or contrast injections, but are often limited by temporal resolution, scan time, or vessel selectivity.^{17,18} Furthermore, due to mixing of non-opacified blood (DSA and contrast-enhanced MRI) and transit time signal decays (ASL), these methods may not be amenable to imaging of venous structures.

There is a growing interest in treating cerebrovascular malformations using a venous approach, making the visualization and evaluation of venous flow patterns even

more essential.¹⁹ Streamlines generated from 4D-flow MRI may help to address these limitations by providing a more flexible means for selective blood-flow tracking, as they can also be applied in reverse, hence tracking the blood from a draining vein backward to the feeding artery. The use of 4D-flow MRI data allows for the possibility of easily seeding venous structures and retrospectively analyzing hemodynamics in vessels of interest, which may increase diagnostic insights and improve pretreatment planning. If viable, improved streamlines from 4D-flow MRI data may be a useful noninvasive vessel tracking option that overcomes the procedural risks associated with DSA and the low temporal nature of other MRI-based methods.

However, in practice, particle tracing with cranial 4D-flow MRI is usually limited to short segments, because 4D-flow MRI velocity fields contain deterministic and stochastic errors that can degrade the length and overall quality of calculated streamlines. One significant deterministic error is displacement artifact, which occurs when acceleration of blood velocities leads to misregistration of velocity and spatial encoding.^{20–22} Such errors can accumulate and become significant when integrated over streamlines, particularly along vessel curves or in stenotic regions where radial and tangential accelerations are present. The principle stochastic error is noise that can lead to nonzero translations of each streamline step.^{23,24} Collectively, these errors may cause streamlines to leave vessel boundaries and terminate, which is especially problematic in the brain due to a higher prevalence of long, narrow, and tortuous vessels. Correction methods have been independently developed to address both displacement^{22,25} and stochastic errors^{26,27} specific to 4D-flow MRI. Additionally, fluid constraints, such as kinetic energy and vessel boundary constraints, can be exploited to further improve streamline visualizations.

This work aims to integrate (1) 3D displacement corrections, (2) probabilistic streamlines, and (3) two novel fluid constraints using time-averaged 4D-flow MRI data. The intent is to provide a processing platform that enables improved selective blood-flow tracking for assessing vessel connectivity and allows for “reverse flow tracking” in clinically meaningful scenarios. In this work, correction methods are validated both in silico

and in vivo and demonstrated in clinical pathology cases.

2 | METHODS

2.1 | Displacement corrections

In phase-contrast MRI, displacement artifacts occur due to the finite temporal spacing between the effective velocity encoding (t_e) and positional encoding (TE), commonly referred to as the displacement time, $t_d = (TE - t_e)$.^{21,28,29} Velocity measurements resulting from moving spins will thus be “displaced” in the reconstructed image. These velocity displacement errors accumulate and cause streamlines to drift, most notably in areas of high vessel curvature. However, because the displacement times can be computed from the applied gradient waveforms, such artifacts can be corrected to some degree.

Several correction methods have been proposed, including a single-step displacement correction method proposed by Steinman et al.²² This method uses reverse streamlines to back-project a displaced velocity value by a step length equal to the velocity at a given point multiplied by the computed displacement time. Later, Thunberg et al proposed an iterative displacement correction method in which the correction process is repeated multiple times until the solution converges to a velocity field consistent with the streamline displacement estimates.²⁵ Both correction methods were validated and compared in an in silico flow model, described in a later section.

2.2 | Probabilistic streamlines

The position of a streamline at point k is given by

$$\mathbf{r}_k = \mathbf{r}_0 + \sum_{j=0}^{k-1} \mathbf{s}_j, \quad (1)$$

where \mathbf{r}_0 is an arbitrary seed location in the data set, and k is the number of streamline step iterations.³ Discrete streamline steps \mathbf{s}_j are calculated by integrating the 3D velocity field over a discrete sampling time δt . In its simplest form, this can be performed with Euler’s method, as follows:

$$\mathbf{s}_j = \mathbf{v}_j \cdot \delta t, \quad (2)$$

However, multistage integration schemes like the fourth-order Runge-Kutta method are commonly used to more accurately calculate streamline steps.³⁰

If measurement uncertainty is considered due to velocity noise for each streamline step, the probability distribution of a local step at spatial location \mathbf{r}_j can be defined as $p_\sigma(\mathbf{s}_j|\mathbf{r}_j)$. From this, the probability of a full streamline (terminating at point \mathbf{r}_k) can be factorized into independent probability distributions, as follows:

$$p(\mathbf{r}_k) = p_\sigma(\mathbf{s}_0, \dots, \mathbf{s}_{k-1}) = \prod_{j=0}^{k-1} p_\sigma(\mathbf{s}_j|\mathbf{r}_j), \quad (3)$$

which describes a *probabilistic* streamline. Equation 3 can then be analyzed with sequential Monte-Carlo sampling, where instead of calculating a step \mathbf{s}_j , a step $\tilde{\mathbf{s}}_j$ is sampled from $p_\sigma(\mathbf{s}_j|\mathbf{r}_j)$. This process can be repeated to produce a large number of probabilistic streamlines (eg, 10 000) to visualize the distribution of possible flow trajectories.

This approach was originally developed for diffusion tensor tractography but has recently been applied to 4D-flow MRI by Friman et al.²⁶ In their work, a local Gaussian probability distribution function was estimated from a covariance matrix using magnitude data from each separate velocity encode. Alternatively, a global Gaussian distribution can be approximated based on expected velocity noise (σ_v) from background tissue. In this study, $p_\sigma(\mathbf{s}_j|\mathbf{r}_j)$ was assumed to be a Gaussian distribution of constant velocity variance, $N(\mathbf{s}_j, \sigma_v)$.

2.3 | Fluid constraints

In this work, we incorporated additional probabilities from two novel fluid constraints after sampling a step $\tilde{\mathbf{s}}_j$ from $p_\sigma(\mathbf{s}_j|\mathbf{r}_j)$. For the first constraint, it was assumed that streamline steps were more likely to fall within higher angiogram values near the center of vessels and less likely to fall within lower angiogram values near the vessel wall. This constraint can be physiologically interpreted as a boundary constraint, encouraging streamlines to stay within the vessel. Angiograms were computed as normalized complex difference³¹ signal amplitudes, and for each proposed step, a probability was calculated based on the new proposed location in the angiogram, as follows:

$$p_{CD} = CD(\mathbf{r}_j + \% \tilde{\mathbf{s}}_j) \in [0, 1]. \quad (4)$$

The second added constraint involved minimizing changes in kinetic energy to restrict streamlines from sudden accelerations (ie, sudden changes in trajectory), which may occur with noisy data or when a streamline leaves a vessel. It can be shown that changes in kinetic energy are proportional to squared changes in step lengths, as follows:

$$\Delta KE = \frac{1}{2}m|\mathbf{v}_j^2 - \mathbf{v}_{j-1}^2| = \frac{1}{2}m\left|\left(\frac{\mathbf{s}_j}{\delta t}\right)^2 - \left(\frac{\mathbf{s}_{j-1}}{\delta t}\right)^2\right| \propto |\mathbf{s}_j^2 - \mathbf{s}_{j-1}^2|. \quad (5)$$

To create a probability, squared differences in step length were normalized and subtracted from unity, as follows:

$$p_{KE} = 1 - \frac{|\% \tilde{\mathbf{s}}_j^2 - \mathbf{s}_{j-1}^2|}{|\% \tilde{\mathbf{s}}_j^2 + \mathbf{s}_{j-1}^2|} \in [0, 1]. \quad (6)$$

Both probabilities from each fluid constraint were multiplied, and a minimum cutoff probability λ was empirically established. If $p_{CD} \cdot p_{KE} > \lambda$, then the random sample step $\tilde{\mathbf{s}}$ was accepted. However, if $p_{CD} \cdot p_{KE} < \lambda$, then $\tilde{\mathbf{s}}$ was rejected and was resampled from $p_{\sigma}(\mathbf{s}_j|\mathbf{r}_j) = N(\mathbf{s}_j, \sigma_v)$ and again tested against the combined probabilities. This process was repeated n times until a suitable sample step was found. Alternatively, if no steps were found, the streamline was terminated. For this study, an n of 90 and λ of 0.6 provided the best results after testing multiple values.

2.4 | In silico

2.4.1 | Study design

To test the effects of displacement corrections, a stenotic U-bend phantom (Figure 1) was created using a non-pulsatile computational fluid dynamics simulation in Fluent (ANSYS, Canonsburg, PA, USA). The simulation was modeled using a Newtonian fluid with the following physical parameters: pipe diameter = 25 mm, curvature radius = 52.5 mm, stenosis diameter = 10 mm, and spatial resolution = 1.39 mm. Data from the U-bend phantom was imported to *MATLAB* (v2020b; MathWorks, Natick, MA, USA) for analysis. With the digitally simulated 3D velocity fields, displacement artifacts were modeled by projecting velocity values forward in time corresponding to three representative displacement times: 2.0, 5.0, and 8.0 ms. Although the displacement times are longer than expected for a typical MRI sequence, it should be noted that displacements scale dimensionally with velocity and that these displacement times were chosen to create sufficient displacements for testing. Displaced velocities were converted to k-space by performing a discrete Fourier transform, and complex Gaussian noise was added in k-space to achieve SNR values of 5, 15, and 40 to test the effects of noise on correction methods. The data were then converted back to image space and velocity fields were corrected using single-step²² and iterative²⁵ displacement-correction

methods discussed previously. For the correction process, velocity values were back-projected using the same displacement times that were used in displacing the original velocity field. Note that these times would be calculated a priori based on pulse-sequence gradient timings. Additionally, it was assumed that displacement artifacts occurred uniformly in all three directions, because the 4D-flow MRI pulse sequence used in human subjects was a 3D radial sequence.^{32,33} Numerical integration of velocity vectors for streamline calculations was performed using a fourth-order Runge-Kutta method and cubic interpolation. A non-probabilistic streamline was generated from each of the 305 voxels spanning the cross-sectional area of a single slice through the vessel inlet (Figure 1A). The length and number of streamlines were assessed 14 mm from the phantom outlet, downstream from the stenosis. Peak velocity in the vessel was 100 cm/s with a velocity encoding set to 120 cm/s.

2.4.2 | Analysis

The effectiveness of both the single-step and iterative displacement correction methods was assessed by comparing the corrected velocity fields to the original (non-displaced) computational fluid dynamics velocity data set. Specifically, errors in magnitude and angle of velocity vectors within the U-bend phantom were computed using RMS error. Errors were also assessed in a displaced data set that was not corrected for displacement artifacts. To quantify streamline quality, average streamline length was computed over all generated streamlines, and the percentage of streamlines reaching the vessel outlet was calculated.

2.5 | Graphical user interface

A graphical user interface was created in *Python* 3.6 to simplify streamline seeding and parameter selection for in vivo experiments. For streamline seeding, 2D planes or 3D spherical regions could be interactively placed over static sagittal and axial maximum intensity projection angiogram images. Both the width and radius of these seeding regions could be adjusted in the parameter selection interface. Functionality for interactive global thresholding of the complex difference angiogram was implemented to create maps for starting constraints (viable seeding areas within vessels). A user-defined number of seed points were randomly placed within seeding regions. Streamlines could then be selected to move in either the forward or reverse directions (by inverting each streamline step) for anterograde and retrograde virtual injections, respectively.

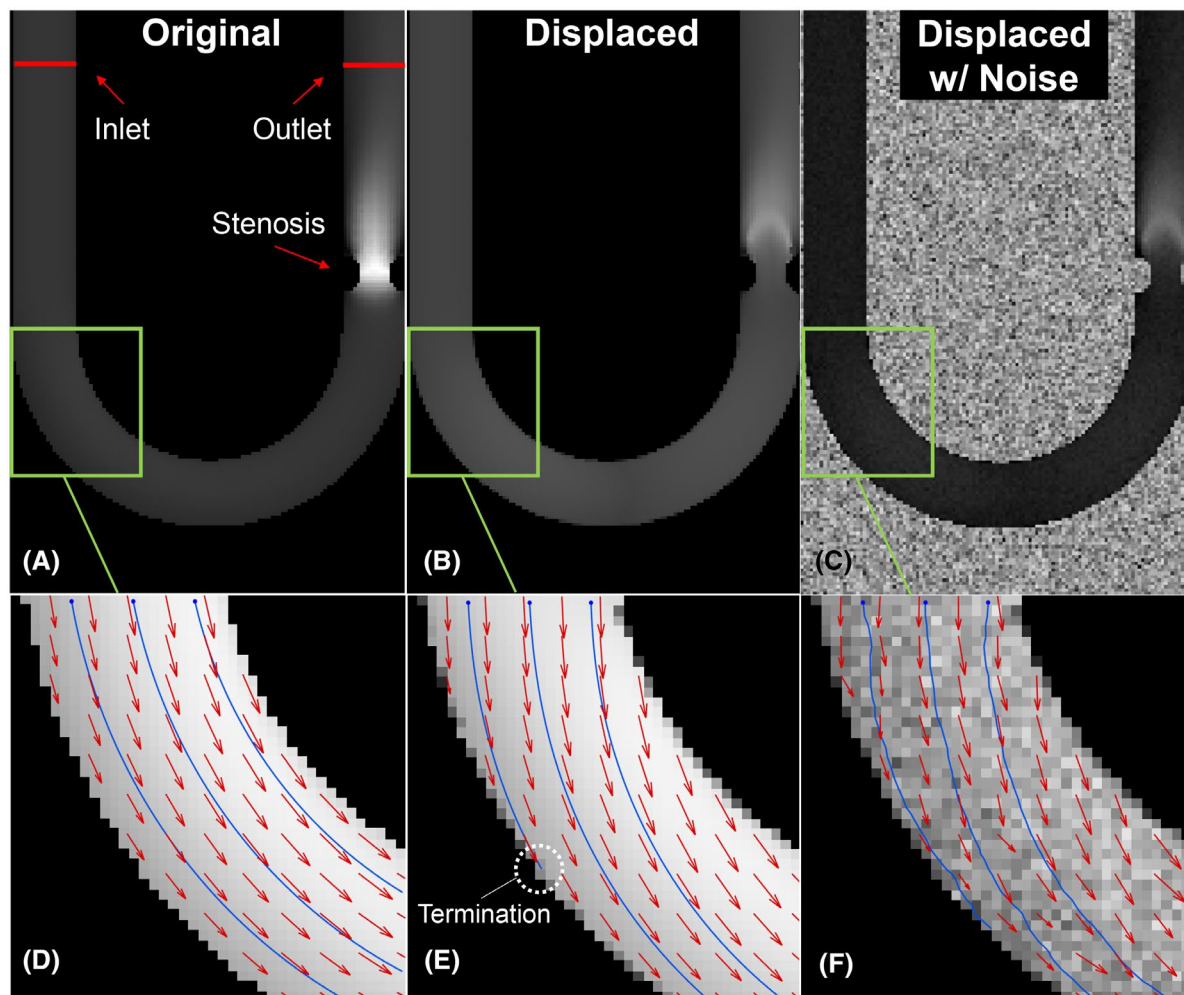


FIGURE 1 Velocity magnitude images from the computation fluid dynamics simulation showing a midsection slice of the U-bend phantom with no displacement (A), simulated displacement of 8 ms (B), and simulated displacement of 8 ms with added noise (C). D–F, Magnified sections of curvature showing in-plane velocity vectors and three streamlines. (E) It can be seen that displacement artifacts from radial acceleration lead streamlines prematurely into the vessel wall. (F) The random effects of noise on streamline trajectories can also be seen

2.6 | In vivo volunteers

2.6.1 | Study design

Ten healthy volunteers (females = 8; mean age = 56.4 years; age range = 48–67 years) were imaged after obtaining written informed consent and approval from the institutional review board. Data were acquired on a clinical 3T MRI system (MR750; GE Healthcare, Waukesha, WI, USA) with a 32-channel head coil using a 3D radially undersampled PC-VIPR (phase contrast vastly undersampled isotropic projection reconstruction) sequence^{32,33} with the following parameters: TR/TE = 7.7/2.7 ms; flip angle = 8°; number of projections = 11 000; acquired spatial resolution = 0.69 mm isotropic; imaging volume = 22 × 22 × 10 cm³; reconstructed matrix size = 320 × 320 × 320; undersampling factor of 14.6 with respect to Nyquist; scan time

= 6 minutes; V_{ENC} = 80 cm/s; and encode scheme = 4-point referenced. A time-averaged 4D-flow reconstruction was performed with parallel imaging with localized sensitivities reconstruction to reduce the spread of undersampling artifacts,³⁴ Maxwell term phase offset corrections,³⁵ 4D Laplacian unwrapping to automatically correct velocity aliasing,³⁶ and third-order polynomial background phase correction.³⁷ Time-averaged velocity images were used for streamline generation, as well as time-averaged magnitude and complex difference datasets.

To assess the effects of deterministic and stochastic streamline correction methods, three sets of streamlines were generated using (1) no displacement correction (uncorrected), (2) iterative displacement correction, and (3) iterative displacement correction with probabilistic streamlines and fluid constraints (iDC+PS+C). The displacement time used for correction was 2.4 ms. To

estimate σ_v , the SD of time-averaged velocity within static brain tissue (after background phase correction) was obtained. This value was then scaled by the ratio of signal magnitudes within vessels due to higher intravascular signal relative to background tissue. Each probabilistic streamline step was perturbed by a vector randomly sampled from $N(\mathbf{s}_j, \sigma_v)$ and constrained by probabilities in Eqs. 4 and 6. Streamlines were seeded in the left and right internal carotid artery (ICA; C1 segment) using spherical seeding regions from the graphical user interface with empirically chosen parameters ($N_p = 10\,000$; step size = 2.0 ms; $N_s = 1000$ steps). The ICAs were chosen because they have high velocity magnitudes and are particularly prone to displacement errors due to their tortuous morphology.

2.6.2 | Analysis

Average streamline lengths and SDs were measured, as well as the number of streamlines crossing planes at the following locations: (1) the terminal portion of the ICA approximately 1 cm before bifurcation, (2) the M1 segment of the middle cerebral artery (MCA) halfway between the ICA bifurcation and the start of the M2 segment, and (3) the A1 segment of the anterior cerebral artery (ACA) halfway between the ICA bifurcation and the start of the A2 segment. Percentage of streamlines crossing these planes was computed by combining the number of streamlines from the right and left sides and normalizing by the number of initial streamlines (20 000 total). The locations of the ICA, MCA, and ACA planes were determined from a 3D visualization of the masked angiogram. Streamline lengths and SDs were compared across each of the three streamline generation methods using one-way repeated-measures analysis of variance tests in SPSS (IBM, Armonk, NY, USA). Paired *t*-tests with Bonferroni corrections were used for pairwise comparisons. Similarly, the number of streamlines reaching ICA, MCA, and ACA were compared using non-parametric Friedman's tests due to the nonnormal distribution of the data (assessed through Shapiro-Wilk tests). Wilcoxon signed-rank tests with Bonferroni corrections were used for pairwise comparisons. Statistical significance was defined as $p < .05$.

2.7 | In vivo clinical subjects

2.7.1 | Study design

To demonstrate the utility of improved streamlines in clinical applications, 3 subjects with intracranial pathology were imaged and analyzed after institutional review board approval and obtaining written informed consent.

This cohort included 1 subject (age = 52 years, female) with a dural arteriovenous fistula (DAVF), 1 subject (age = 19 years, female) with an arteriovenous malformation (AVM), and 1 subject (age = 70 years, female) with an intracranial aneurysm. Magnetic resonance imaging data were acquired on a clinical 3T system (MR750; GE Healthcare, Waukesha, WI) with a eight-channel head coil using a 3D radially undersampled PC-VIPR sequence (9,10) using the following parameters: TR/TE = 8.1/2.7 ms; flip angle = 15°; number of projections = 10 000; spatial resolution = 0.69 mm isotropic; imaging volume = $22 \times 22 \times 10$ cm³; reconstructed matrix size = $320 \times 320 \times 320$; undersampling factor of 16.1 with respect to Nyquist; scan time = 6.5 minutes; $V_{ENC} = 100$ cm/s; and encode scheme = 5-point balanced.³⁸ The same time-averaged 4D-flow reconstruction algorithms and streamline parameters used in the volunteer experiments were used for these subjects. For all 3 clinical subjects, "virtual injections" were obtained using improved streamlines (displacement corrections and probabilistic streamlines with fluid constraints). Additionally, for the subject with an intracranial aneurysm, a dynamic 3D radial pseudo-continuous ASL (PCASL) exam was acquired.^{39,40}

2.7.2 | Aneurysm

Forward virtual injections were generated by seeding a 2D plane at the C1 level of the ICA. The number of probabilistic streamlines was increased to 20 000 to account for the large seeding area. To qualitatively compare dynamic PCASL and 4D-flow streamlines, grayscale coronal maximum intensity projections of streamline density were created and matched to PCASL delay times. Plane location for seeding and slab sizes were also matched between the two imaging methods.

2.7.3 | Dural arteriovenous fistula

An initial evaluation of the DAVF was performed using DSA (internal and external carotid injections) at an outside institution by a board-certified neurointerventionalist with reinterpretation of the imaging findings by a trained neuroradiologist with 26 years of experience (PAT). A follow-up 4D-flow MRI was then performed. To evaluate flow patterns in the DAVF, selective antegrade virtual injections were generated in the left transverse sinus and superior sagittal sinus. Four-dimensional flow-derived pressure maps were also obtained to assess differences in intravascular pressure.⁴¹ A secondary evaluation was then performed by the same neuroradiologist using virtual injections and pressure maps.

2.7.4 | Arteriovenous malformation

To demonstrate the visualization and seeding capabilities of the graphical user interface, three virtual injections were generated in the left ICA, right ICA, and basilar artery with three separate colors. The number of streamline steps (N_s) was extended to 1800 to assess whether streamlines persisted into the venous system. Next, an initial assessment of AVM inflow and outflow tracks was performed by creating simultaneous forward and reverse virtual injections within the nidus. From this, two sets of retrograde virtual injections were then generated in each draining vein to visualize the portion of the nidus supplied by each vein and to qualitatively demonstrate respective filling rates within the nidus. Volumetric flow rates were obtained from 4D-flow data to corroborate observed filling rates from retrograde flow tracking.

3 | RESULTS

3.1 | In silico

Table 1 lists the computed RMS error in velocity vector magnitude and angle between each displacement correction method and the ground-truth (nondisplaced) image. Both correction methods improved velocity field errors; however, it was observed that a significant amount of error still existed near vessel boundaries. Table 1 also provides average streamline length and percentage of streamlines crossing the phantom outlet. Both metrics of streamline quality improved upon performing displacement correction. For the single-step

correction, RMS error values were lower relative to the iterative method only in scenarios with low SNR and small displacement times. However, at moderate and high SNRs and displacement times, RMS error was lowest using iterative displacement corrections. Furthermore, all metrics of streamline quality were consistently greater with iterative displacement corrections. Figure 2 shows streamlines generated with an SNR of 15 and displacement time of 5 ms with ground-truth, uncorrected (displaced), and displacement corrected data sets. Improvements in streamline quality can be observed when using iterative displacement correction methods relative to single-step; however, both correction methods improved streamline quality relative to no displacement correction.

3.2 | In vivo volunteers

Streamlines were successfully generated in all 10 subjects. The mean estimated velocity noise within vessels was 0.77 ± 0.15 cm/s. Figure 3 shows streamlines generated in 1 volunteer using each of the three correction methods. Qualitatively, it was observed that streamline length (and depth into vasculature) increased as deterministic and stochastic corrections were added. Streamlines were longest when using displacement corrections and constrained probabilistic streamlines and filled the vasculature more completely. To further demonstrate this, Supporting Information Video S1 shows time-resolved virtual injections in another volunteer in axial, coronal, and sagittal views. Figure 4 shows box plots of streamline length, SD in streamline length, and percentage of streamlines passing the ICA

TABLE 1 Velocity error and streamline quality measurements in silico

SNR	t_d	Angular RMSE (degrees)			Magnitude RMSE (cm/s)			Passing Outlet (%)			Length (mm)		
		Disp.	ssDC	iDC	Disp.	ssDC	iDC	Disp.	ssDC	iDC	Disp.	ssDC	iDC
5	2	16.35	8.38	8.64	0.093	0.051	0.054	16.2	13.4	25.6	163.8	138.4	187.9
	5	16.71	8.05	7.76	0.103	0.055	0.048	9.5	31.2	52.1	139.2	157.0	224.1
	8	17.05	8.37	7.76	0.110	0.076	0.050	0.3	30.2	43.0	106.9	159.8	213.7
15	2	7.76	2.27	2.28	0.042	0.015	0.012	50.1	53.1	64.9	239.9	220.6	265.5
	5	8.54	2.04	2.02	0.061	0.031	0.011	10.8	53.4	69.5	183.8	217.4	275.2
	8	9.35	2.50	2.08	0.075	0.054	0.014	0.7	41.6	64.3	155.2	201.2	271.0
40	2	7.24	1.24	1.23	0.041	0.010	0.007	50.8	53.4	69.5	235.7	223.8	277.4
	5	8.25	1.24	1.17	0.061	0.029	0.006	10.8	52.8	68.2	190.4	218.6	277.1
	8	8.94	2.12	1.23	0.075	0.054	0.011	0.0	39.7	69.2	156.4	207.9	276.3

Note: Bold signifies the best-performing method for each metric.

Abbreviations: Disp., displaced (no correction); iDC, iterative displacement correction; RMSE, RMS error; ssDC, single-step displacement correction; t_d , displacement time (ms).

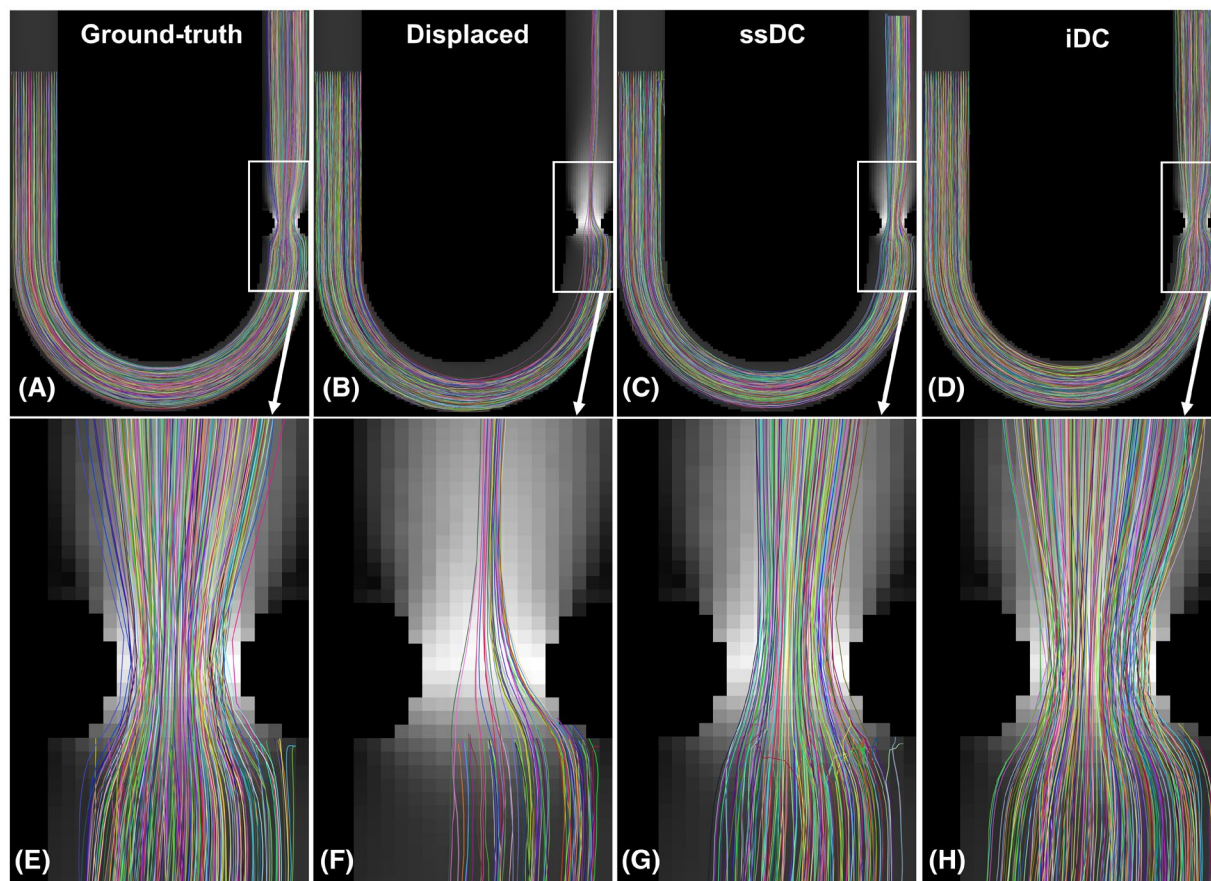


FIGURE 2 Streamlines ($N_p = 305$) generated from ground-truth (A), displaced (B), single-step displacement corrected (ssDC) (C), and iterative displacement corrected (iDC) (D) data sets. Shown are randomly colored streamlines projected onto the middle slice of the 3D U-bend phantom. (E–H) Magnified sections of the stenosis demonstrate improvements after performing displacement corrections

and entering the MCA and ACA for each correction method. After performing separate repeated-measures analysis of variance tests with Greenhouse-Geisser corrections, there were significant differences in mean streamline length ($F[1.17,10.54] = 88.48$; $p = 1.00^{-06}$) and SD in streamline lengths ($F[1.19,10.66] = 114.31$; $p = 2.93^{-07}$) across methods. Similarly, Friedman's tests revealed significant differences in number of streamlines exiting the ICA before bifurcation (chi-square = 20.00; $p = 4.50e-05$), number of streamlines entering the MCA (chi-square = 20.00; $p = 4.50^{-05}$), and a number of c-parametric and nonparametric post hoc tests demonstrated significant differences between each method after correction for multiple comparisons. When using displacement corrections and constrained probabilistic streamlines, an average of 37.3% of initial streamlines were measured at the C7 segment of the ICA, indicating a 62.7% loss in streamlines along the ICA. Similarly, a combined average of 27.0% of initial streamlines was measured in the ACA and MCA, reflecting a 10.3% loss of streamlines at the ICA bifurcation.

3.3 | In vivo clinical subjects

3.3.1 | Aneurysm

Figure 5 shows virtual injections (using displacement corrections and constrained probabilistic streamlines) alongside dynamic PCASL images. Comparison to PCASL resulted in good qualitative agreement and clear delineation of the ACA intracranial aneurysm between the two imaging methods. While the improved streamline method reduced image noise, there was decreased visualization of smaller intracranial vessels.

3.3.2 | Dural arteriovenous fistula

The DSA and 4D-flow data both demonstrated a left transverse sinus DAVF with left ascending pharyngeal, left posterior branch of the middle meningeal, and left occipital feeding arteries. The DSA images of a left external carotid injection (Figure 6A) showed a small amount of reflux of contrast medium from the ipsilateral left

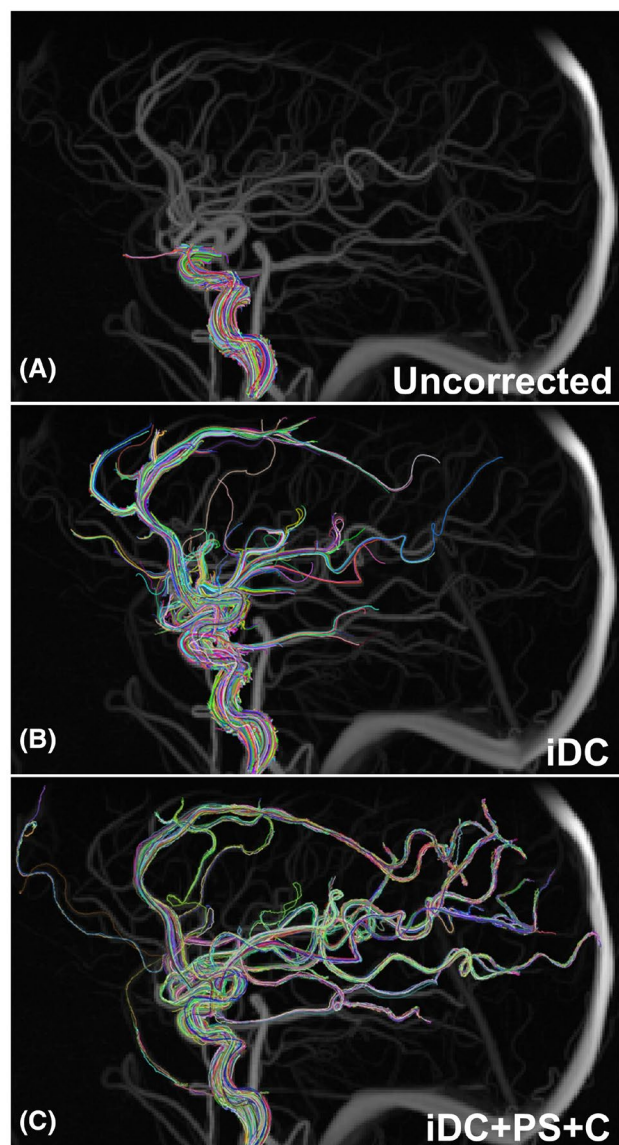


FIGURE 3 Randomly colored streamlines seeded in the left and right internal carotid arteries (10 000 total) in a volunteer showing the results after no correction (A), iterative displacement correction (iDC) only (B), and after iterative displacement correction (C) with probabilistic streamlines and fluid constraints (iDC+PS+C). Streamlines are projected along the sagittal dimension and overlaid on complex difference angiogram maximum intensity projections. Note the improvements in streamline visualizations as deterministic and stochastic corrections are added, allowing smaller branching arteries to be seen

transverse into the contralateral right transverse sinus. This resulted in an initial DAVF grading of Cognard type IIA. However, it was unclear what role the bolus injection contributed to the observed reflux. The 4D-flow MRI pressure maps (Figure 6B) revealed increased intravascular pressure within the left transverse sinus. Using virtual injections (Figure 6C), retrograde flow can be visualized in the left transverse sinus with anterograde

flow in the superior sagittal sinus and right transverse sinus. Virtual injections provide simultaneous views of both intracranial and extracranial flow contributions to the right transverse sinus not possible with DSA. The initial grading was confirmed after evaluating the 4D-flow data sets.

3.3.3 | Arteriovenous malformation

Figure 7 and Supporting Information Video S2 show three sets of multicolor virtual injections, selectively seeded in the ICAs and basilar artery. It was observed that increasing the number of streamline steps allowed some streamlines to persist into venous structures, namely, the superior sagittal sinus and transverse sinuses. Figure 8 and Supporting Information Video S3 show both anterograde (blue) and retrograde (red) simultaneous flow tracking in the nidus of a temporoparietal AVM. All feeding arteries (retrograde) and draining veins (anterograde) were well-visualized. However, selective microcatheter DSA imaging did not allow for complete visualization of the venous compartments due to the inflow of nonopacified blood from communicating vessels. Figure 9 and Supporting Information Video S4 clearly show the two draining veins that were seeded individually using retrograde, dual-color virtual injections. Faster retrograde filling of the nidus was observed in the larger vein, indicating faster flow and more dominant drainage through the nidus. Slower flow was seen in the smaller vein, which was better accentuated with dual-seeding assessment compared with Figure 8. To corroborate these findings, average volumetric flow rates and vessel areas were successfully obtained from 4D-flow MRI data. Flow in the larger draining was 2.09 mL/s with a vessel area of 12.1 mm², while flow in the smaller draining vein was 0.33 mL/s with an area of 7.0 mm².

4 | DISCUSSION

In this study, a method for generating “virtual injections” with improved streamlines was developed by integrating displacement corrections, probabilistic streamlines, and novel fluid constraints. Displacement corrections were first validated in silico with a computational fluid dynamics simulation, and the addition of stochastic corrections with fluid constraints was tested in a cohort of 10 healthy volunteers. Virtual injections were then applied to a small number of clinical subjects to evaluate intracranial vascular pathology.

Considerations for acceleration-induced displacement errors have traditionally been limited to tangential accelerations, as seen in stenoses, where such errors can

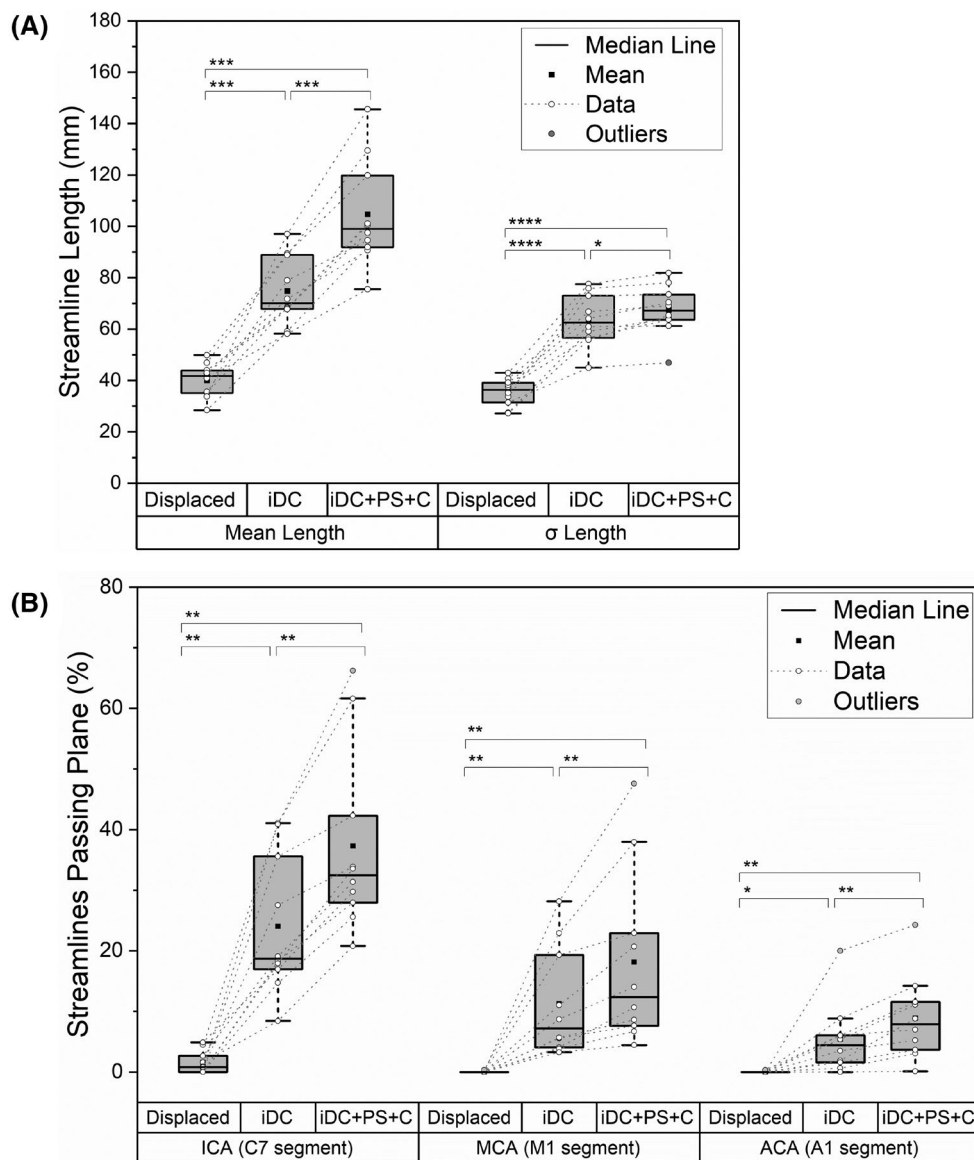


FIGURE 4 A, Box plots comparing mean streamline length and SD of streamline lengths among each of the three tested methods: uncorrected (displaced), iterative displacement correction (iDC), and iterative displacement correction with probabilistic streamlines and fluid constraints (iDC+PS+C). (B) Box plots showing the percentage of streamlines passing specific locations along the vasculature using each of the three methods. Cut planes were placed in the C7 segment of the internal carotid artery (ICA), M1 segment of the middle cerebral artery (MCA), and A1 segment of the anterior cerebral artery (ACA). For both sets of box plots, dashed lines are drawn across each method to indicate paired data points for a single subject. *p*-Values for post hoc tests are indicated by asterisks: **p* ≤ .05; ***p* ≤ .01; ****p* ≤ .001; *****p* ≤ .0001

be easily identified and may significantly alter flow-rate measurements.^{22,29} However, it was shown that displacement artifacts due to radial acceleration also cause significant errors, particularly when the errors are compounded across a streamline trajectory. In this study, it was demonstrated that previously proposed displacement correction methods targeted toward tangential accelerations also work well for correcting radial accelerations.

While the probabilistic streamlines described by Friman et al²⁶ represent an accurate mathematical Monte-Carlo modeling of noise and can be used to quantify probability

for a set of streamline steps, the improved probabilistic streamlines presented in this paper use kinetic energy and vessel boundary constraints, which are themselves susceptible to error, making the probabilistic interpretation less clear. We instead view them as an improvement in qualitative visualization of blood flow, allowing streamlines to extend through the entire vasculature to provide characterization of flow pathways. Traditional streamlines are usually constrained to exist only within vessel boundaries created from masked angiograms, as is typically done in diffusion tensor tractography.⁴² The method presented

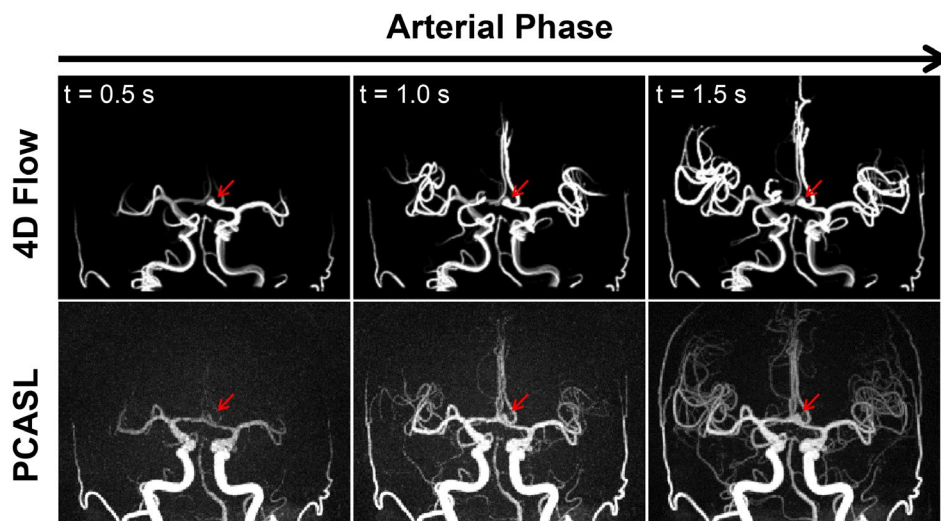


FIGURE 5 Comparison of virtual injections generated from improved streamlines from 4D-flow MRI and dynamic pseudo-continuous arterial spin labeling (PCASL) in a subject with an aneurysm in the anterior communicating artery (red arrow). Temporal frames for both data sets were matched, with arterial phase increasing from left to right. For both 3D images, data were projected along the coronal dimension. Note that signal intensities in the virtual injection images are directly proportional to the local streamline density at each specific time frame. Good qualitative agreement is seen between the two data sets

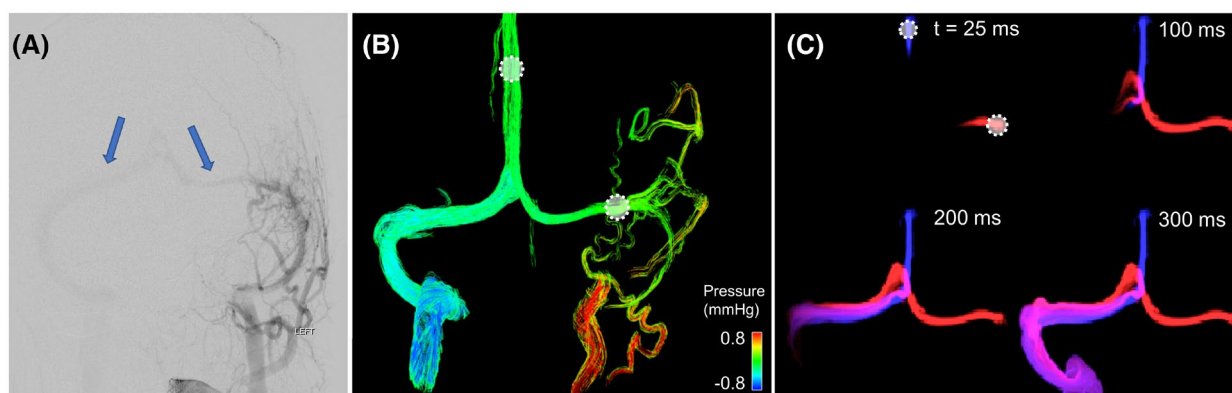


FIGURE 6 A, Digital subtraction angiography (DSA) image of a left external carotid injection showing a left transverse sinus dural arteriovenous fistula (DAVF) and potential reflux (arrows) into the right transverse sinus. B, The 4D-flow MRI-derived pressure mapping in the dural sinuses indicates increased intravascular pressure within the left transverse sinus. The two dashed circles represent seed point locations for streamline generation. C, Selective anterograde virtual injections in the superior sagittal sinus (blue) and left transverse sinus (red) are shown at four time frames. Note the retrograde flow away from the DAVF, corroborating results from DSA

here differs significantly because there is no global threshold; the angiogram is simply used as an additional probability with no hard cutoff. This allows streamlines to track through smaller vessels that may be masked out with a conservative global threshold.

As evidenced in volunteers and clinical subjects, the use of displacement corrections and probabilistic streamlines with fluid constraints greatly increase the overall length of streamlines as well as their depth into the vascular tree. It was shown that streamlines seeded in the internal carotid arteries and basilar artery can even propagate into venous structures when using a large number of streamline steps. However, as observed in the volunteer

study, there was still a significant loss of streamlines along the length of the ICA and some loss at the ICA bifurcation. While it may be expected that streamlines be conserved in a perfectly measured velocity field, there are stochastic and deterministic errors present in the velocity field, numerical integration errors, and probabilistic streamline steps that cause streamlines to leave the vessel boundary and ultimately terminate.

In comparison to dynamic PCASL, virtual injections had increased temporal resolutions (limited to the streamline temporal step size δt) and offered a notable reduction in image noise. However, these benefits were partially offset by some loss in visualization of smaller-diameter vessel

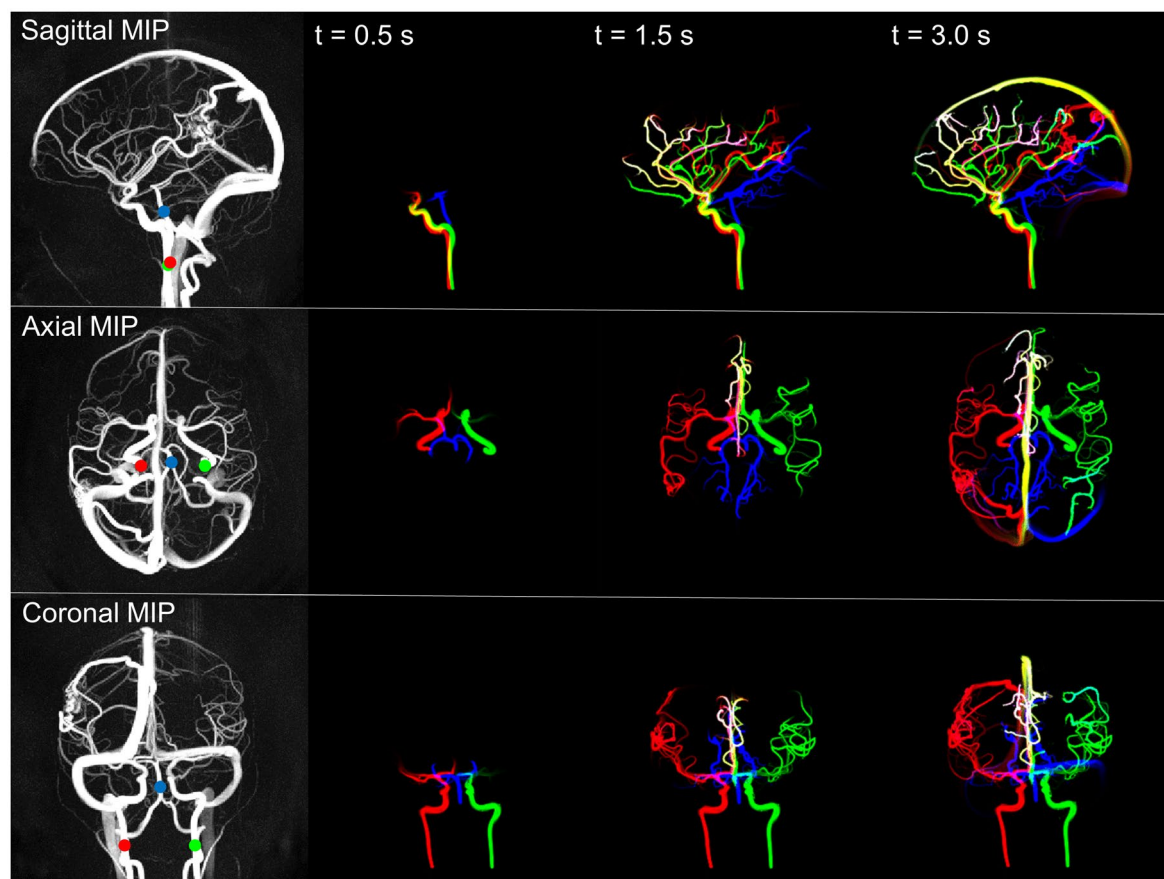


FIGURE 7 (Left) Sagittal, axial, and coronal maximum intensity projections (MIPs) of 4D-flow complex difference angiograms in a subject with a temporoparietal arteriovenous malformation. Seed locations in the left internal carotid (green), right internal carotid (red), and basilar (blue) arteries are depicted by colored points on the angiogram. (Right) Colored streamlines generated from the three seed locations over increasing arterial phase (left to right). Note the propagation of streamlines into the venous system at the latest time frame, and the convergence of blood pathways shown as color mixing in yellow and white

structures. Importantly, the results were qualitatively similar between both modalities, and the intracranial aneurysm was well-visualized in both sets of images. It should also be noted that the administration of contrast agents may also further improve visualization of small vessels by improving angiogram and velocity data quality, which has been shown in other studies.⁴³

The use of 4D-flow MRI for generating streamlines provides multiple benefits. First, by obtaining one 4D-flow data set, streamlines can be retrospectively generated at any vessel location within the 3D imaging volume. This is particularly beneficial when evaluating venous structures; arterial injection imaging methods are often prone to mixing of nonopacified blood. Furthermore, streamlines can be generated at multiple seed locations, allowing for targeted flow tracking in any number of vessels with multicolor representation. Second, in addition to forward streamlines, reverse streamlines can be created by inverting each streamline step. This was particularly useful for identifying feeding arteries in an AVM and for assessing filling rates of draining veins in the same AVM (which

were poorly visualized on DSA). Defining venous compartments, as well as their high and low flow components, would be clinically valuable for preprocedural venous embolization planning and would add to the global AVM assessment before arterial embolization. Third, 4D-flow MRI can provide additional quantitative hemodynamic measures, such as volumetric flow rate, arterial pulsatility, intravascular pressure, and wall shear stress, among others.⁴⁴ These metrics, which have been validated and tested in various intracranial pathologies, can further assist in comprehensive hemodynamic assessments. Finally, 4D-flow MRI is noninvasive, and recent advances in image acceleration have allowed 4D-flow scans to be performed in relatively short scan times (eg, the 6-minute PCVIPR sequence used in this study).

As stated previously, although the fluid constraints are based on realistic physiological assumptions, the theoretical underpinnings and statistical interpretation of such constraints applied to probabilistic streamlines have not yet been fully established. Despite this limitation, our improved streamline approach was shown experimentally

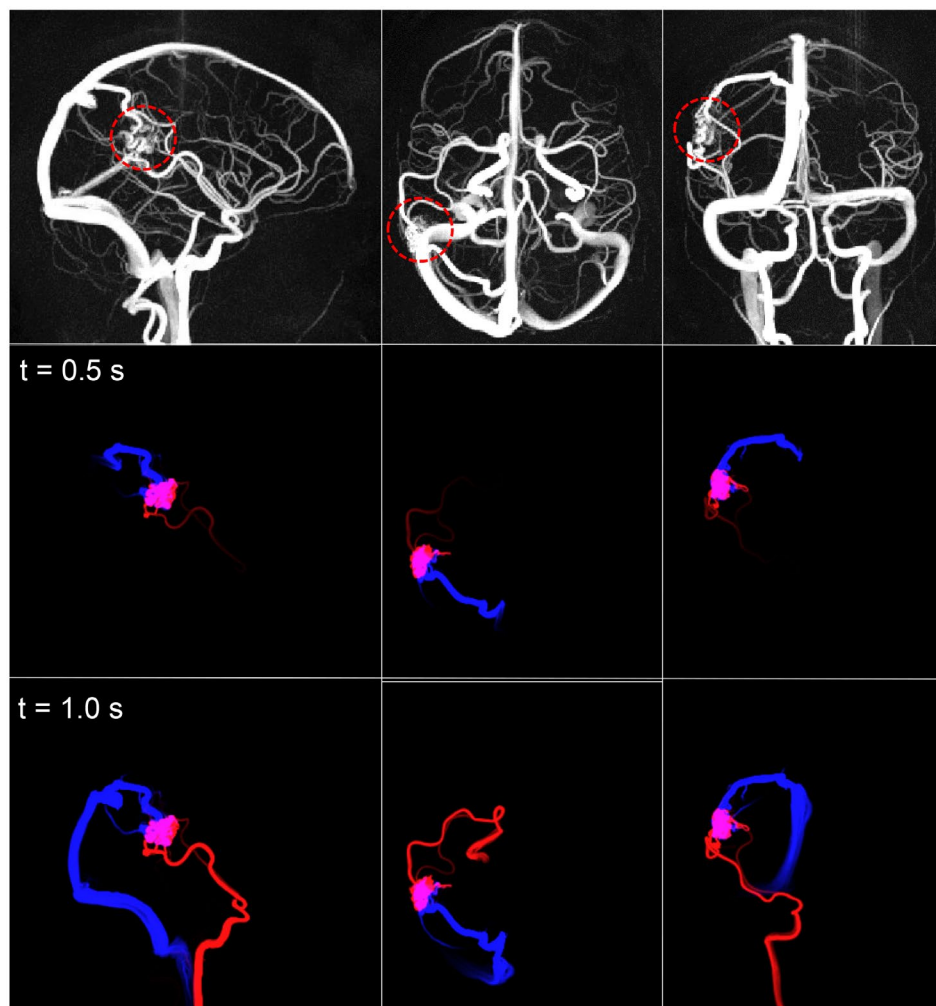


FIGURE 8 (Top) Sagittal, axial, and coronal MIPs of the complex difference angiogram. The nidus of the temporoparietal arteriovenous malformation (dashed red circle) was seeded with both forward and reverse streamlines. (Bottom) Anterograde (blue) and retrograde (red) virtual injections depict feeding arteries and draining veins over increasing time frames

to have excellent visual agreement with dynamic PCASL. However, some caution should be taken in interpreting our virtual injection approach as a physiologically accurate modeling of a true “injection,” which would require consideration of, for example, fluid–tissue interactions, blood density, diffusion, and pressure changes from an injection. One interesting consideration would be obtaining and using intravoxel velocity distributions,⁴⁵ which would allow for “contrast” dispersion, or to represent equal streamline density by considering the flux of fluid through each voxel—an approach that has been used in mapping vector fields for MRI coil design.⁴⁶

Although displacement times can be calculated analytically from gradient waveforms, they may not represent the optimal displacement time for corrections, particularly if velocity fields are underestimated or overestimated by higher orders of motion. It is possible to measure the optimal correction displacement time by testing various displacement times and finding the value that produces

an optimal correction, although this might suffer from overfitting problems. In this study, displacement times along each encoding direction were equivalent due to the 3D radial acquisition, simplifying the correction process. However, this could easily be extended to Cartesian acquisitions, in which the displacement times would not be the same along each encoding direction.

Computation times for generating virtual injections were approximately 85 minutes. A large portion of this time was dedicated to 3D interpolation when computing probabilities for the vessel boundary constraint. Currently, the implementation is far from optimal performance, and significant gains could be achieved by calculating streamlines in parallel, cropping large imaging volumes, using faster interpolation methods, and use of GPU processing. Faster computation times would more easily facilitate testing different parameters (eg, minimum cutoff probability, discrete sampling time), which were chosen empirically. This would likely be necessary when using different

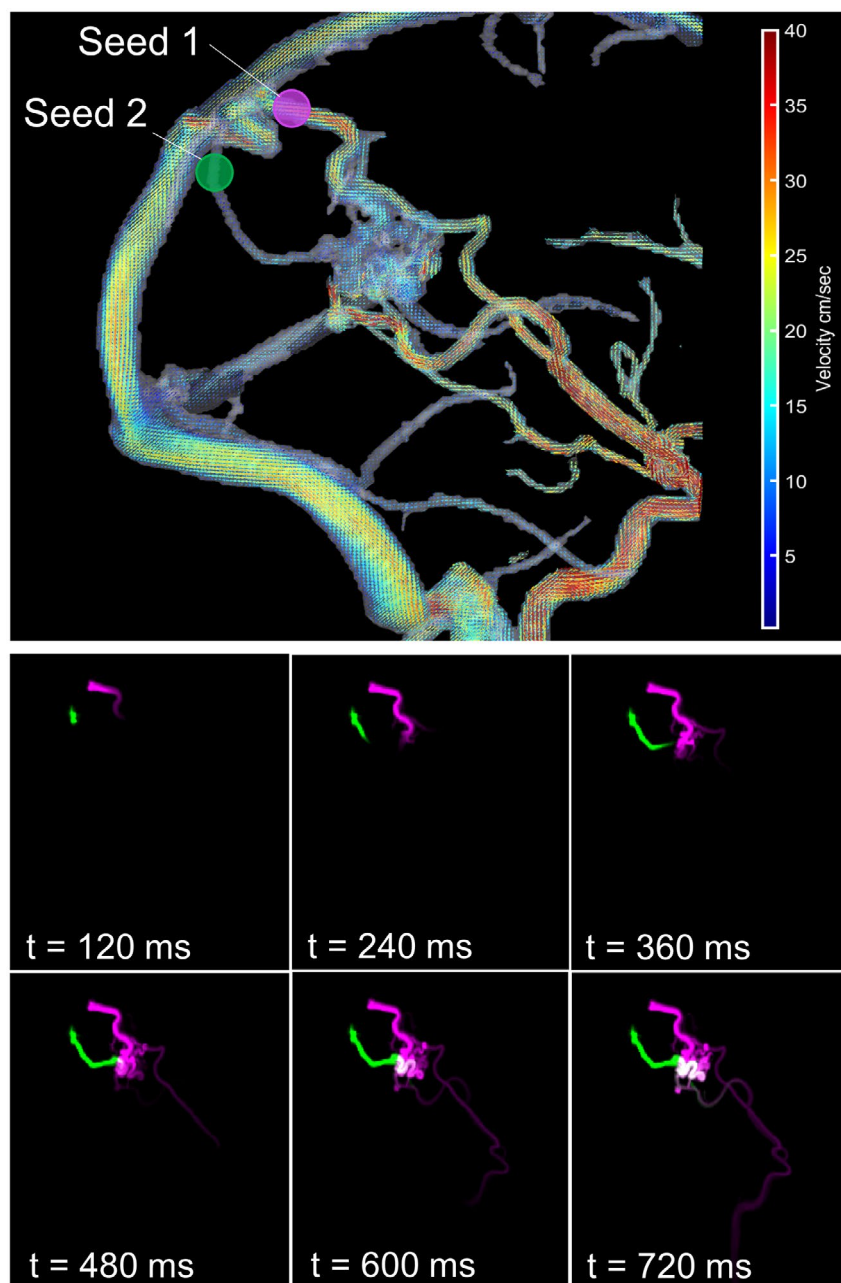


FIGURE 9 (Top) The 4D-flow visualization of velocity vectors color-coded by velocity magnitude (in centimeters per second) near a temporoparietal arteriovenous malformation. Draining veins, identified in the anterograde/retrograde flow tracking assessment, were seeded separately with reverse streamlines at the locations identified by “Seed 1” and “Seed 2.” (Bottom) Retrograde virtual injections in the smaller draining vein (green) and larger draining vein (purple). Filling rates from each draining vein can be observed over increasing time frames

spatial resolutions, introducing contrast agents, using other preprocessing steps (eg, denoising), or applying virtual injections to different clinical applications.

Although data in this study were sampled for time-resolved reconstructions (10 000 projections over a 6-minute scan session), only time-averaged velocity data sets were used to increase SNR and decrease computational load. It is possible that reducing the number of projections may still provide high data quality while reducing scan times. However, 4D-flow MRI acquisitions can provide dynamic data and methods for time-resolved probabilistic pathlines have been described previously and can be adapted into our current code.²⁶ With the increasing prevalence of constrained reconstruction and higher temporal resolutions, frame-by-frame accelerations in blood

velocities may also need to be considered in 4D-flow MRI data sets with higher pulsatility.²² Finally, velocity noise is approximated globally based on SD of velocity in background tissue. More rigorous methods for computing velocity noise on a voxel-by-voxel basis should be considered, such as by creating a covariance matrix using magnitude data from each separate velocity encode.

Future work seeks to quantitatively compare DSA, contrast-enhanced MRA, and dynamics ASL techniques. Methods for computing time-of-arrival maps have been proposed for these modalities^{40,47,48} and can be readily applied to 4D-flow MRI virtual injections. The numerical phantom used in this study was modeled to resemble aortic dimensions and morphology. Future work looks to consider an ICA model with similar spatial

resolutions as to those acquired in vivo. Additionally, future work looks to apply well-known divergence-free algorithms^{24,49–51} to further reduce stochastic noise in 4D-flow velocity data. Finally, larger clinical studies are needed to evaluate the impact of virtual injections on intracranial vascular malformation management and patient outcomes.

5 | CONCLUSIONS

This work demonstrated the efficacy of highly constrained probabilistic streamlines that allow for robust blood-flow tracking along tortuous and lengthy vessel paths that are present in the brain. This was accomplished by isolating two errors that are not commonly addressed in 4D-flow MRI: displacement artifacts and noise. By presenting improved methods of addressing these errors, in combination with novel fluid constraints, it was shown that improved visualizations of the vasculature in the brain could be obtained. With the additional flexibility in streamline direction, seeding location, and color representation, as well as potential use of other hemodynamic parameters from 4D-flow MRI, virtual injections may be a valuable method for characterizing and diagnosing cerebrovascular malformations.

ACKNOWLEDGMENTS

The authors thank Dr. Sebastian Kozerke and Dr. Christian Binter at ETH Zurich for providing the computation fluid dynamics dataset used in this study. They also thank GE Healthcare for their continued technical assistance and product support. The content is solely the responsibility of the authors and does not necessarily represent the official views of these institutions.

DATA AVAILABILITY STATEMENT

Python code from this study is openly available at the following repository: <https://github.com/groberts1/Virtual-Injection>.

ORCID

Grant S. Roberts  <https://orcid.org/0000-0003-1472-4352>

Michael W. Loecher  <https://orcid.org/0000-0002-6533-1113>

Kevin M. Johnson  <https://orcid.org/0000-0002-8660-0853>

Laura B. Eisenmenger  <https://orcid.org/0000-0001-6764-4239>

Oliver Wieben  <https://orcid.org/0000-0002-7931-1930>

REFERENCES

1. Markl M, Frydrychowicz A, Kozerke S, Hope M, Wieben O. 4D flow MRI. *J Magn Reson Imaging*. 2012;36:1015-1036.
2. Buonocore MH. Visualizing blood flow patterns using streamlines, arrows, and particle paths. *Magn Reson Med*. 1998;40:210-226.
3. Napel S, Lee DH, Frayne R, Rutt BK. Visualizing three-dimensional flow with simulated streamlines and three-dimensional phase-contrast MR imaging. *J Magn Reson Imaging*. 1992;2:143-153.
4. Markl M, Kilner PJ, Ebbers T. Comprehensive 4D velocity mapping of the heart and great vessels by cardiovascular magnetic resonance. *J Cardiovasc Magn Reson*. 2011;13:7.
5. Bogren HG, Buonocore MH, Follette DM. Four-dimensional aortic blood flow patterns in thoracic aortic grafts. *J Cardiovasc Magn Reson*. 2000;2:201-208.
6. Geiger J, Markl M, Jung B, et al. 4D-MR flow analysis in patients after repair for tetralogy of Fallot. *Eur Radiol*. 2011;21:1651-1657.
7. Bammer R, Hope TA, Aksoy M. Time-resolved AMT. 3D quantitative flow MRI of the major intracranial vessels: initial experience and comparative evaluation at 1.5T and 3.0T in combination with parallel imaging. *Magn Reson Med*. 2007;57:127-140.
8. Hope MD, Purcell DD, Hope TA, et al. Complete intracranial arterial and venous blood flow evaluation with 4D flow MR imaging. *Am J Neuroradiol*. 2009;30:362-366.
9. Edjlali M, Roca P, Rabrait C, et al. MR selective flow-tracking cartography: a postprocessing procedure applied to four-dimensional flow MR imaging for complete characterization of cranial dural arteriovenous fistulas. *Radiology*. 2014;270:261-268.
10. Schnell S, Ansari SA, Vakil P, et al. Three-dimensional hemodynamics in intracranial aneurysms: influence of size and morphology. *J Magn Reson Imaging*. 2014;39:120-131.
11. Liu J, Koskas L, Faraji F, et al. Highly accelerated intracranial 4D flow MRI: evaluation of healthy volunteers and patients with intracranial aneurysms. *MAGMA*. 2018;31:295-307.
12. Robson PM, Dai W, Shankaranarayanan A, Rofsky NM, Alsop DC. Time-resolved vessel-selective digital subtraction MR angiography of the cerebral vasculature with arterial spin labeling. *Radiology*. 2010;257:507-515.
13. Cashen TA, Jeong H, Shah MK, et al. 4D radial contrast-enhanced MR angiography with sliding subtraction. *Magn Reson Med*. 2007;58:962-972.
14. Lee C-C, Reardon MA, Ball BZ, et al. The predictive value of magnetic resonance imaging in evaluating intracranial arteriovenous malformation obliteration after stereotactic radiosurgery. *J Neurosurg*. 2015;123:136-144.
15. Howard BM, Hu R, Barrow JW, Barrow DL. Comprehensive review of imaging of intracranial aneurysms and angiographically negative subarachnoid hemorrhage. *Neurosurg Focus*. 2019;47:E20.
16. Kaufmann TJ, Huston J 3rd, Mandrekar JN, Schleck CD, Thielen KR, Kallmes DF. Complications of diagnostic cerebral angiography: evaluation of 19,826 consecutive patients. *Radiology*. 2007;243:812-819.
17. Hadizadeh DR, Kukuk GM, Steck DT, et al. Noninvasive evaluation of cerebral arteriovenous malformations by 4D-MRA for preoperative planning and postoperative follow-up in 56 patients: comparison with DSA and intraoperative findings. *Am J Neuroradiol*. 2012;33:1095.

18. Jezzard P, Chappell MA, Okell TW. Arterial spin labeling for the measurement of cerebral perfusion and angiography. *J Cereb Blood Flow Metab.* 2017;38:603-626.
19. Chen C-J, Norat P, Ding D, et al. Transvenous embolization of brain arteriovenous malformations: a review of techniques, indications, and outcomes. *Neurosurg Focus.* 2018;45:E13.
20. Oshinski JN, Ku DN, Bohning DE, Pettigrew RI. Effects of acceleration on the accuracy of MR phase velocity measurements. *J Magn Reson Imaging.* 1992;2:665-670.
21. Frayne R, Rutt BK. Understanding acceleration-induced displacement artifacts in phase-contrast MR velocity measurements. *J Magn Reson Imaging.* 1995;5:207-215.
22. Steinman DA, Ethier CR, Rutt BK. Combined analysis of spatial and velocity displacement artifacts in phase contrast measurements of complex flows. *J Magn Reson Imaging.* 1997;7:339-346.
23. Andersen AH, Kirsch JE. Analysis of noise in phase contrast MR imaging. *Med Phys.* 1996;23:857-869.
24. Song SM, Napel S, Glover GH, Pelc NJ. Noise reduction in three-dimensional phase-contrast MR velocity measurements. *J Magn Reson Imaging.* 1993;3:587-596.
25. Thunberg P, Wigstrom L, Ebbers T, Karlsson M. Correction for displacement artifacts in 3D phase contrast imaging. *J Magn Reson Imaging.* 2002;16:591-597.
26. Friman O, Hennemuth A, Harloff A, Bock J, Markl M, Peitgen HO. Probabilistic 4D blood flow tracking and uncertainty estimation. *Med Image Anal.* 2011;15:720-728.
27. Loecher M, Kecskemeti S, Turski P, Wieben O. Comparison of divergence-free algorithms for 3D MRI with three-directional velocity encoding. *J Cardiovasc Magn Reson.* 2012;14(Suppl 1):W64.
28. Simonetti OP, Wendt RE 3rd, Duerk JL. Significance of the point of expansion in interpretation of gradient moments and motion sensitivity. *J Magn Reson Imaging.* 1991;1:569-577.
29. Thunberg P, Wigstrom L, Wranne B, Engvall J, Karlsson M. Correction for acceleration-induced displacement artifacts in phase contrast imaging. *Magn Reson Med.* 2000;43:734-738.
30. Darmofal DL, Haimes R. An analysis of 3D particle path integration algorithms. *J Comput Phys.* 1996;123:182-195.
31. Bernstein MA, Ikezaki Y. Comparison of phase-difference and complex-difference processing in phase-contrast MR angiography. *J Magn Reson Imaging.* 1991;1:725-729.
32. Gu T, Korosec FR, Block WF, et al. PC VIPR: a high-speed 3D phase-contrast method for flow quantification and high-resolution angiography. *Am J Neuroradiol.* 2005;26:743-749.
33. Johnson KM, Lum DP, Turski PA, Block WF, Mistretta CA, Wieben O. Improved 3D phase contrast MRI with off-resonance corrected dual echo VIPR. *Magn Reson Med.* 2008;60:1329-1336.
34. Griswold MA, Jakob PM, Nittka M, Goldfarb JW, Haase A. Partially parallel imaging with localized sensitivities (PILS). *Magn Reson Med.* 2000;44:602-609.
35. Bernstein MA, Zhou XJ, Polzin JA, et al. Concomitant gradient terms in phase contrast MR: analysis and correction. *Magn Reson Med.* 1998;39:300-308.
36. Loecher M, Schrauben E, Johnson KM, Wieben O. Phase unwrapping in 4D MR flow with a 4D single-step laplacian algorithm. *J Magn Reson Imaging.* 2016;43:833-842.
37. Walker PG, Cranney GB, Scheidegger MB, Waseleski G, Pohost GM, Yoganathan AP. Semiautomated method for noise reduction and background phase error correction in MR phase velocity data. *J Magn Reson Imaging.* 1993;3:521-530.
38. Johnson KM, Markl M. Improved SNR in phase contrast velocimetry with five-point balanced flow encoding. *Magn Reson Med.* 2010;63:349-355.
39. Wu H, Block WF, Turski PA, Mistretta CA, Johnson KM. Noncontrast-enhanced three-dimensional (3D) intracranial MR angiography using pseudocontinuous arterial spin labeling and accelerated 3D radial acquisition. *Magn Reson Med.* 2013;69:708-715.
40. Wu H, Block WF, Turski PA, et al. Noncontrast dynamic 3D intracranial MR angiography using pseudo-continuous arterial spin labeling (PCASL) and accelerated 3D radial acquisition. *J Magn Reson Imaging.* 2014;39:1320-1326.
41. Rivera-Rivera LA, Johnson KM, Turski PA, Wieben O. Pressure mapping and hemodynamic assessment of intracranial dural sinuses and dural arteriovenous fistulas with 4D flow MRI. *Am J Neuroradiol.* 2018;39:485-487.
42. Smith RE, Tournier JD, Calamante F, Connelly A. Anatomically-constrained tractography: improved diffusion MRI streamlines tractography through effective use of anatomical information. *NeuroImage.* 2012;62:1924-1938.
43. Bock J, Frydrychowicz A, Stalder AF, et al. 4D phase contrast MRI at 3 T: effect of standard and blood-pool contrast agents on SNR, PC-MRA, and blood flow visualization. *Magn Reson Med.* 2010;63:330-338.
44. Stalder AF, Russe MF, Frydrychowicz A, Bock J, Hennig J, Markl M. Quantitative 2D and 3D phase contrast MRI: optimized analysis of blood flow and vessel wall parameters. *Magn Reson Med.* 2008;60:1218-1231.
45. Dyverfeldt P, Sigfridsson A, Kvitting J-PE, Ebbers T. Quantification of intravoxel velocity standard deviation and turbulence intensity by generalizing phase-contrast MRI. *Magn Reson Med.* 2006;56:850-858.
46. While PT, Forbes LK. Equi-flux streamline seeding for three-dimensional vector fields. *J Eng Math.* 2012;76:81-100.
47. Ruedinger KL, Schafer S, Speidel MA, Strother CM. 4D-DSA: development and current neurovascular applications. *Am J Neuroradiol.* 2021;42:214.
48. Schubert T, Wu Y, Johnson KM, et al. Time-of-arrival parametric maps and virtual bolus images derived from contrast-enhanced time-resolved radial magnetic resonance angiography improve the display of brain arteriovenous malformation vascular anatomy. *Invest Radiol.* 2016;51:706-713.
49. Ong F, Uecker M, Tariq U, et al. Robust 4D flow denoising using divergence-free wavelet transform. *Magn Reson Med.* 2015;73:828-842.
50. Santelli C, Loecher M, Busch J, Wieben O, Schaeffter T, Kozerke S. Accelerating 4D flow MRI by exploiting vector field divergence regularization. *Magn Reson Med.* 2016;75:115-125.
51. Busch J, Giese D, Wissmann L, Kozerke S. Reconstruction of divergence-free velocity fields from cine 3D phase-contrast flow measurements. *Magn Reson Med.* 2013;69:200-210.

SUPPORTING INFORMATION

Additional supporting information may be found in the online version of the article at the publisher's website.

VIDEO S1 Time-resolved virtual injections for a healthy volunteer using displacement corrections and constrained

probabilistic streamlines shown in axial, coronal, and sagittal views. Signal intensities in each pixel are proportional to streamline density

VIDEO S2 Animation of Figure 7 showing a virtual injection with multicolor representation. Three sets of improved streamlines were seeded in the left internal carotid (green), right internal carotid (red), and basilar (blue) arteries

VIDEO S3 Animation of Figure 8 showing a virtual injection seeded in the nidus of an arteriovenous malformation with simultaneous anterograde (blue) and retrograde (red) blood tracking

VIDEO S4 Animation of Figure 9 showing a virtual injection with selective seeding in the dominant (purple) and smaller (green) draining veins of an arteriovenous malformation

How to cite this article: Roberts GS, Loecher MW, Spahic A, et al. Virtual injections using 4D flow MRI with displacement corrections and constrained probabilistic streamlines. *Magn Reson Med*. 2022;87:2495–2511. doi:[10.1002/mrm.29134](https://doi.org/10.1002/mrm.29134)